# Parity violation in atomic ytterbium: Experimental sensitivity and systematics

K. Tsigutkin,[1,*] D. Dounas-Frazer,[1] A. Family,[1] J. E. Stalnaker,[1,†] V. V. Yashchuk,[2] and D. Budker[3]

[1]*Department of Physics, University of California at Berkeley, Berkeley, California 94720-7300, USA*

[2]*Advanced Light Source Division, Lawrence Berkeley National Laboratory, Berkeley, California 94720, USA*

[3]*Nuclear Science Division, Lawrence Berkeley National Laboratory, Berkeley, California 94720, USA*

(Received 4 January 2010; published 12 March 2010)

We present a detailed description of the observation of parity violation in the $^1S_0$-$^3D_1$ 408-nm forbidden transition of ytterbium, a brief report of which appeared earlier. Linearly polarized 408-nm light interacts with Yb atoms in crossed $E$ and $B$ fields. The probability of the 408-nm transition contains a parity-violating term, proportional to $(\mathcal{E} \cdot \mathbf{B})[(\mathbf{E} \times \mathcal{E}) \cdot \mathbf{B}]$, arising from interference between the parity-violating amplitude and the Stark amplitude due to the $E$ field ($\mathcal{E}$ is the electric field of the light). The transition probability is detected by measuring the population of the $^3P_0$ state, to which 65% of the atoms excited to the $^3D_1$ state spontaneously decay. The population of the $^3P_0$ state is determined by resonantly exciting the atoms with 649-nm light to the $6s7s\,^3S_1$ state and collecting the fluorescence resulting from its decay. Systematic corrections due to $E$-field and $B$-field imperfections are determined in auxiliary experiments. The statistical uncertainty is dominated by parasitic frequency excursions of the 408-nm excitation light due to the imperfect stabilization of the optical reference with respect to the atomic resonance. The present uncertainties are 9% statistical and 8% systematic. Methods of improving the accuracy for future experiments are discussed.

     PACS number(s): 11.30.Er, 32.90.+a

## I. INTRODUCTION

In an earlier paper [1], we reported on the observation of the atomic parity-violation (PV) effect in the $6s^2\,^1S_0 \to 5d6s\,^3D_1$ 408-nm forbidden transition of $^{174}$Yb. We measured the PV-induced transition matrix element to be $8.7 \pm 1.4 \times 10^{-10} e\,a_0$, which confirms the theoretically anticipated parity-violation enhancement in Yb [2] and constitutes the largest atomic PV effect observed so far. However, the measurement accuracy is not yet sufficient for the observation of the isotopic and hyperfine differences in the PV amplitude, the study of which is the main goal of the present experiments. Here we describe the impact of the apparatus imperfections and systematic effects on the accuracy of the measurements and discuss ways of improving it.

During the initial stage of the experiment, an effort was invested into measuring various spectroscopic properties of the Yb system of direct relevance to the PV measurement, including radiative lifetimes, Stark-induced amplitudes, hyperfine structure, isotope shifts, and dc Stark shifts of the $6s^2\,^1S_0 \to 5d6s\,^3D_1$ transition [3]. In addition, the $6s^2\,^1S_0 \to {}^3D_2$ transition at 404 nm has been observed, and the electric quadrupole transition amplitude and tensor transition polarizability have been measured [4]. The forbidden magnetic-dipole ($M1$) amplitude of the 408-nm transition was measured to be $1.33 \times 10^{-4}\mu_B$ using the $M1$-(Stark-induced)$E1$ interference technique [5]. The ytterbium atomic system, where transition amplitudes and interferences are well understood, has proven useful for gaining insight into the Jones-dichroism effects that have been studied in condensed-matter systems at extreme conditions and whose origins

have been a matter of debate (see Ref. [6] and references therein).

An experimental and theoretical study of the dynamic (ac) Stark effect on the $6s^2\,^1S_0 \to 5d6s\,^3D_1$ forbidden transition was also undertaken [7]. A model was developed to calculate spectral line shapes resulting from resonant excitation of atoms in an intense standing light wave in the presence of off-resonant ac Stark shifts. A by-product of this work was an independent determination (from the saturation behavior of the 408-nm transition) of the Stark transition polarizability, which was found to be in agreement with the earlier measurement [4].

The present Yb atomic parity violation (APV) experiment involves a measurement using an atomic beam. An alternative approach would involve working with a heat-pipe-like vapor cell. Various aspects of such an experiment were investigated, including measurements of collisional perturbations of relevant Yb states [8], nonlinear optical processes in a dense Yb vapor with pulsed UV-laser excitation [9], and an altogether different scheme for measuring APV via optical rotation on a transition between excited states [10].

The present paper addresses the issues of sensitivity and systematics in the Yb APV experiment. In Secs. II and III the experimental technique and its application in the present experiment are discussed. In Sec. IV a method of analyzing the impact of various apparatus imperfections is described based on theoretical modeling of signals recorded by the detection system in the presence of imperfections. In Sec. V a detailed description of the experimental apparatus is given, along with a discussion of the origins of the imperfections, which is followed by an account of the measurements of the imperfections in Sec. VI. In Secs. VII and VIII we discuss measurements and analysis of the PV amplitude and systematic effects, and ways of improving the accuracy of the PV measurements to better than 1% in order to measure the difference in the APV effects between different isotopes and hyperfine components.

---

*[\*]tsigutkin@berkeley.edu

[†]Present address: Department of Physics and Astronomy, Oberlin College, Oberlin, Ohio 44074, USA.
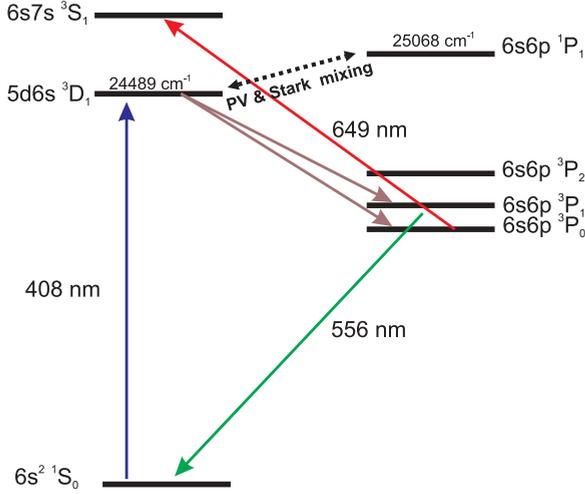
FIG. 1. (Color online) Low-lying energy eigenstates of Yb and transitions relevant to the APV experiment.

## II. EXPERIMENTAL TECHNIQUE FOR THE APV MEASUREMENT

As discussed in Ref. [1], the idea of the experiment is to excite the forbidden 408-nm transition (Fig. 1) with resonant laser light in the presence of a quasistatic electric field. The PV amplitude of this transition arises due to PV mixing of the $5d6s\,^3D_1$ and $6s6p\,^1P_1$ states. The purpose of the electric field is to provide a reference transition amplitude, which is due to Stark mixing of the same states interfering with the PV amplitude. In such an interference method [11,12], one is measuring the part of the transition probability that is linear in both the reference Stark-induced amplitude and the PV amplitude. In addition to enhancing the PV dependent signal, the Stark-PV interference technique provides for all-important reversals that separate the PV effects from the systematics.

Even though the APV effect in Yb is relatively large, and the $M1$ transition is strongly suppressed, the $M1$ transition amplitude is still three orders of magnitude larger than the PV amplitude. As a result, the geometry of the experiment was designed to suppress spurious $M1$-Stark interference. In addition, this effect is minimized by the use of a power buildup cavity to generate a standing light wave. Since a standing wave has no net direction of propagation, any transition rate which is linear in the $M1$ amplitude, will cancel out (see below).

The advantages of the present experimental configuration can be demonstrated by considering Yb atoms in the presence of static electric, **E**, and magnetic, **B**, fields interacting with a standing monochromatic wave produced by two counter-propagating coherent waves in an optical cavity. The electric field in the standing wave, $\mathcal{E}$, is a sum of the fields of the two waves. For resonant atoms, the transition rate from the ground state $^1S_0$ to the excited state $^3D_1$ is [see, e.g., [13], Eq. (3.127)]

$$R_M = \frac{4}{\hbar^2 \Gamma} |A_M|^2, \tag{1}$$

where $\Gamma$ is the natural linewidth of the transition, $A_M$ is the transition amplitude, and $M = 0, \pm 1$ is the magnetic quantum number of the excited state. Here and in the rest of this section,

it is assumed that the individual magnetic sublevels of the $^3D_1$ state are resolved. For convenience, we set $\hbar = 1$ henceforth and measure the transition rate in units of $\Gamma$.

The transition amplitude $A_M$ is the sum of the electric ($E1$) and magnetic ($M1$) dipole transition amplitudes:

$$A_M = A_M^{(E1)} + A_M^{(M1)}. \tag{2}$$

The $E1$ amplitude has two contributions corresponding to the Stark and PV mixing of the $^3D_1$ and $^1P_1$ states. That is,

$$\begin{aligned} A_M^{(E1)} &= A_M^{(\mathrm{Stark})} + A_M^{(\mathrm{APV})} \\ &= i\beta(-1)^M (\mathbf{E} \times \boldsymbol{\mathcal{E}})_{-M} + i\zeta(-1)^M \mathcal{E}_{-M}, \end{aligned} \tag{3}$$

where $\beta$ is the vector transition polarizability, $\zeta$ is related to the reduced matrix element of the Hamiltonian describing the weak interaction, and $\mathcal{E}_{0,\pm 1}$ are the spherical components of the vector $\boldsymbol{\mathcal{E}}$. Although Stark-induced transitions are generally characterized by scalar, vector, and tensor polarizabilities [4,11], for the case of a $J = 0 \to 1$ transition, only the vector polarizability contributes. Equation (3) is derived in Appendix A.

Similarly, the $M1$ transition amplitude has two components: one for each of the two counter-propagating laser beams. Let $\boldsymbol{\mathcal{E}}_+ = \mathcal{E}_+ \hat{\boldsymbol{\mathcal{E}}}$ and $\boldsymbol{\mathcal{E}}_- = \mathcal{E}_- \hat{\boldsymbol{\mathcal{E}}}$ denote the electric fields of the beams traveling in the **k** and $-\mathbf{k}$ directions, respectively. Then $\boldsymbol{\mathcal{E}} = \boldsymbol{\mathcal{E}}_+ + \boldsymbol{\mathcal{E}}_-$ and the $M1$ amplitude is given by

$$\begin{aligned} A_M^{(M1)} &= \mathcal{M}(-1)^M (\mathbf{k} \times \boldsymbol{\mathcal{E}}_+)_{-M} + \mathcal{M}(-1)^M (-\mathbf{k} \times \boldsymbol{\mathcal{E}}_-)_{-M} \\ &= \mathcal{M}(-1)^M (\delta \mathbf{k} \times \boldsymbol{\mathcal{E}})_{-M}, \end{aligned} \tag{4}$$

where $\mathcal{M}$ is the reduced matrix element of the $M1$ transition and **k** is a unit vector in the direction of the wave vector. Here we have introduced $\delta \mathbf{k} = \delta k\, \mathbf{k}$ with $\delta k = (\mathcal{E}_+ - \mathcal{E}_-)/\mathcal{E}$. For a perfect standing wave, $\mathcal{E}_+ = \mathcal{E}_-$ and hence $\delta k = 0$ and the $M1$ transition is completely suppressed. In practice, $\mathcal{E}_- = \mathcal{E}_+ - \delta\mathcal{E}$ due to the small but nonzero transmission of the back mirror in the cavity. Since $|\delta\mathcal{E}| \ll \mathcal{E}$, $|\delta k| \approx |\delta\mathcal{E}/\mathcal{E}| \ll 1$. Thus, although the $M1$ transition amplitude is not strictly zero, it is highly suppressed.

Without loss of generality, the quantities $\beta$, $\zeta$, and $\mathcal{M}$ are assumed to be real. In general, the rate $R_M$ given by Eq. (1) includes terms proportional to $\beta\mathcal{M}$ (Stark-$M1$ interference) and $\beta\zeta$ (Stark-PV interference).

A careful choice of field geometry allows for additional suppression of undesirable Stark-$M1$ interference. From Eq. (3), it is evident that the Stark-PV interference is proportional to the rotational invariant

$$(\underbrace{\boldsymbol{\mathcal{E}}}_{\mathrm{PV}} \cdot \mathbf{B})[\underbrace{(\mathbf{E} \times \boldsymbol{\mathcal{E}})}_{\mathrm{Stark}} \cdot \mathbf{B}]. \tag{5}$$

In the present experimental apparatus, the electric field **E** is applied orthogonally to the magnetic field **B** and collinearly with the axis of the linearly polarized standing light wave, as shown in Fig. 2.

This geometry is such that the $M1$ and Stark-induced amplitudes are out of phase. Thus, they do not interfere and therefore do not produce spurious PV-mimicking effects (see Sec. IV).
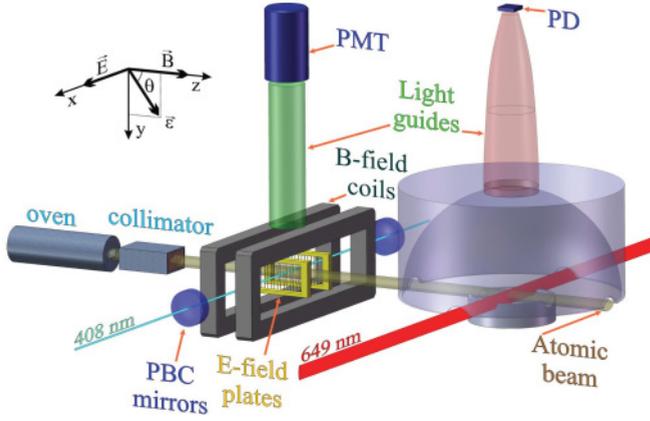
FIG. 2. (Color online) Orientation of fields for PV-Stark interference experiment and schematic of the present APV apparatus. Not shown is the vacuum chamber containing all the depicted elements, except the photomultiplier (PMT) and the photodiode (PD). PBC is the power buildup cavity. Light is applied collinearly with **x**.

### III. PV SIGNATURE: IDEAL CASE

In the ideal case where we neglect the apparatus imperfections, the static magnetic and electric fields are $\mathbf{B} = B\,\hat{\mathbf{z}}$ and $\mathbf{E} = E\,\hat{\mathbf{x}}$, respectively, and the light standing wave has an electric field

$$\boldsymbol{\mathcal{E}} = \mathcal{E}(\sin\theta\,\hat{\mathbf{y}} + \cos\theta\,\hat{\mathbf{z}}). \qquad (6)$$

With this field orientation (see Fig. 2), Eqs. (1)–(4) yield

$$R_0 = 4\mathcal{E}^2(\beta^2 E^2 \sin^2\theta + 2\zeta\,\beta E \sin\theta\cos\theta), \qquad (7)$$

$$R_{\pm 1} = 2\mathcal{E}^2(\beta^2 E^2 \cos^2\theta - 2\zeta\,\beta E \sin\theta\cos\theta), \qquad (8)$$

where terms of order $\zeta^2$ and higher are neglected, and $\delta k = 0$ is assumed.

To isolate the Stark-PV interference term from the dominant Stark-induced transition rate, we modulate the electric field: $E = E_{dc} + \tilde{E}_0 \cos(\omega t)$, where $\tilde{E}_0$ is the modulation amplitude, $\omega$ is the modulation frequency, and $E_{dc}$ provides a dc bias. Then Eqs. (7) and (8) become

$$R_M = \mathcal{R}_M^{[0]} + \mathcal{R}_M^{[1]} \cos(\omega t) + \mathcal{R}_M^{[2]} \cos(2\omega t), \qquad (9)$$

where $\mathcal{R}_M^{[n]}$ is the amplitude of the $n$th harmonic of the transition rate $R_M$. The dominant Stark-induced contribution, which oscillates at twice the modulation frequency, is

$$\mathcal{R}_0^{[2]} = 2\beta^2 \tilde{E}_0^2 \mathcal{E}^2 \sin^2\theta, \qquad (10)$$

$$\mathcal{R}_{\pm 1}^{[2]} = \beta^2 \tilde{E}_0^2 \mathcal{E}^2 \cos^2\theta. \qquad (11)$$

On the other hand, the amplitude $\mathcal{R}_M^{[1]}$ contains the Stark-PV interference term:

$$\mathcal{R}_0^{[1]} = 8\mathcal{E}^2(\beta^2 \tilde{E}_0 E_{dc} \sin^2\theta + \zeta\beta\tilde{E}_0 \sin\theta\cos\theta), \qquad (12)$$

$$\mathcal{R}_{\pm 1}^{[1]} = 4\mathcal{E}^2(\beta^2 \tilde{E}_0 E_{dc} \cos^2\theta - \zeta\beta\tilde{E}_0 \sin\theta\cos\theta). \qquad (13)$$

The term $\mathcal{R}_M^{[0]}$ is a constant "background":

$$\mathcal{R}_0^{[0]} = 4\mathcal{E}^2 \left[\beta^2\left(\tilde{E}_0^2 + E_{dc}^2\right)\sin^2\theta + 4\zeta\beta E_{dc}\sin\theta\cos\theta\right],$$

$$\mathcal{R}_{\pm 1}^{[0]} = 2\mathcal{E}^2 \left[\beta^2\left(\tilde{E}_0^2 + E_{dc}^2\right)\cos^2\theta - 4\zeta\beta E_{dc}\sin\theta\cos\theta\right].$$
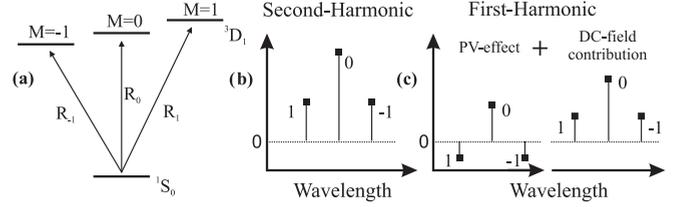


FIG. 3. Discrimination of the PV effect by $E$-field modulation under static magnetic field. The Zeeman pattern is shown for the polarization angle $\theta = \pi/4$.

For an arbitrary polarization angle $\theta$, all three Zeeman components of the transition, as shown in Fig. 3(a), are present while scanning over the spectral profile of the transition. The first-harmonic signal due to Stark-PV interference has a characteristic signature: the sign of the oscillating terms for the two extreme components of the transition is opposite to that of the central component. The second-harmonic signal provides a reference for the line shape since it is free from interference effects linear in **E** [Fig. 3(b)]. With a nonzero dc component present in the applied electric field, a signature identical to that in the second harmonic will also appear in the first harmonic, Fig. 3(c). The latter can be used to increase the first-harmonic signal above the noise, which makes the profile analysis more reliable.

To obtain the PV term from the measured first- and second-harmonic transition rates, we first normalize the first-harmonic signals $\mathcal{R}_M^{[1]}$ by their second-harmonic counterparts $\mathcal{R}_M^{[2]}$ and combine the results in the following way:

$$\mathcal{K} = \frac{\mathcal{R}_{-1}^{[1]}}{\mathcal{R}_{-1}^{[2]}} + \frac{\mathcal{R}_{+1}^{[1]}}{\mathcal{R}_{+1}^{[2]}} - 2\frac{\mathcal{R}_0^{[1]}}{\mathcal{R}_0^{[2]}} = \mp\frac{16\zeta}{\beta\tilde{E}_0}. \qquad (14)$$

Here we take $\theta = \pm\pi/4$, which are optimal polarization angles for the PV measurements (see next section). This method has the advantage that $\mathcal{K}$ is independent of $E_{dc}$, so that the $E$-field bias may be chosen based on technical requirements of the experimental apparatus.

### IV. PV SIGNATURE: IMPACT OF APPARATUS IMPERFECTIONS

While the current Yb-APV apparatus has been designed to minimize systematic effects, the PV mimicking systematics may be a result of a combination of multiple apparatus imperfections. To understand the importance of these effects, the electric and magnetic field misalignments and stray fields were included in a theoretical model of the transition rates as well as the excitation light's deviations from linear polarization. In addition, we relax the assumption that $\delta k = 0$ and include the effects of the residual $M1$ transition.

The quantization axis is defined along $\hat{\mathbf{z}}$, and following the ideal case model, the axis of the standing light wave is collinear with $\hat{\mathbf{x}}$. We added a small ellipticity to the light polarization by taking

$$\boldsymbol{\mathcal{E}} = \mathcal{E}(\hat{\mathbf{y}}\sin\theta + \hat{\mathbf{z}}\,e^{i\phi}\cos\theta), \qquad (15)$$

where $\phi$ is a small phase. For $|\phi| \ll 1$, the ellipticity of the light is $2\phi\sin(2\theta)$. The electric field imperfections are included by

taking

$$\mathbf{E} = \tilde{\mathbf{E}} + \mathbf{E}',$$

where

$$\tilde{\mathbf{E}} = (\tilde{E}_0\hat{\mathbf{x}} + \tilde{e}_y\hat{\mathbf{y}} + \tilde{e}_z\hat{\mathbf{z}})\cos(\omega t),$$
$$\mathbf{E}' = E_{dc}\hat{\mathbf{x}} + e_y\hat{\mathbf{y}} + e_z\hat{\mathbf{z}},$$

are the ac and dc components of the electric field. It is assumed that the $y$ and $z$ components of the ac field are in phase with the leading oscillating $E$ field. The impact of the out-of-phase ac components was analyzed within a complete model of the systematics and found to be negligible. The ac components are due to misalignments of the applied $E$ field with respect to the light wave axis as well as to the quantization axis $\hat{\mathbf{z}}$. The dc components arise due to a misalignment of the dc-bias field and also due to stray electric fields in the interaction region.

The magnetic-field imperfections are defined within the same frame of reference by taking analogously

$$\mathbf{B} = \tilde{\mathbf{B}} + \mathbf{B}',$$

where

$$\tilde{\mathbf{B}} = \tilde{b}_x\hat{\mathbf{x}} + \tilde{b}_y\hat{\mathbf{y}} + B\hat{\mathbf{z}},$$
$$\mathbf{B}' = b'_x\hat{\mathbf{x}} + b'_y\hat{\mathbf{y}} + b'_z\hat{\mathbf{z}},$$

where $\tilde{\mathbf{B}}$ and $\mathbf{B}'$ are reversing and stray nonreversing magnetic fields, respectively.

Equations (1)–(4) apply when the quantization axis is along the magnetic field, thus a rotation $\mathbb{D}$ is applied to each of the vectors $\mathbf{E}$, $\mathbf{B}$, $\mathcal{E}$, and $\mathbf{k}$ such that $\mathbb{D}\mathbf{B} \propto \hat{\mathbf{z}}$. That is, we take

$$\mathbf{B} \to \mathbb{D}\mathbf{B}, \quad \mathbf{E} \to \mathbb{D}\mathbf{E}, \quad \mathcal{E} \to \mathbb{D}\mathcal{E}, \quad \text{and} \quad \mathbf{k} \to \mathbb{D}\mathbf{k}, \quad (16)$$

where

$$\mathbb{D} = \mathscr{D}(-\alpha_y, \hat{\mathbf{y}})\mathscr{D}(\alpha_x, \hat{\mathbf{x}}). \quad (17)$$

Here the matrix $\mathscr{D}(\alpha, \hat{\mathbf{n}})$ represents a rotation about an axis $\hat{\mathbf{n}}$ through angle $\alpha$. The angles $\alpha_x$ and $\alpha_y$ are given by

$$\alpha_{x,y} = (B - b'_z)(b'_{y,x} + \tilde{b}_{y,x})/B^2. \quad (18)$$

Thus, the electric field $\mathbf{E}$ and the polarization vector $\mathcal{E}$ acquire additional components after the rotation (besides, for example, $e_y$ and $\tilde{e}_y$).

Due to the imperfections, the normalized-rate modulation amplitudes now include additional terms besides the Stark and the PV effects:

$$\frac{\mathcal{R}_M^{[1]}}{\mathcal{R}_M^{[2]}} \equiv r_M = r_M^{(Stark)} + r_M^{(APV)} + r_M^{(M1)} + r_M^{(\phi)}, \quad (19)$$

where $r_M^{(Stark)}$ is the Stark contribution due to the dc bias and the field imperfections, $r_M^{(APV)}$ is the PV-Stark-interference term, $r_M^{(M1)}$ is the $M1$-Stark-interference contribution, and $r_M^{(\phi)}$ is a contribution due to the distorted linear polarization of the light (which is a Stark contribution, but we explicitly separate the contribution linear in $\phi$). Expressions for the lowest-order terms are summarized in Table I.

The normalized-amplitude combination (14) has been chosen to determine the PV asymmetry. Since the $M1$

TABLE I. Lowest-order terms contributing to the normalized transition-rate modulation amplitudes $r_M$.

| | $r_M^{(APV)}$ | $r_M^{(M1)}$ | $r_M^{(\phi)}$ |
|---|---|---|---|
| $M = 0$ | $+\dfrac{4\zeta\cot\theta}{\beta\tilde{E}_0}$ | $0$ | $0$ |
| $M = -1$ | $-\dfrac{4\zeta\tan\theta}{\beta\tilde{E}_0}$ | $+\dfrac{4\delta k\,\mathcal{M}(\tilde{e}_y - \tilde{e}_z\tan\theta)}{\beta\tilde{E}_0^2}$ | $+\dfrac{4e_z\phi\tan\theta}{\tilde{E}_0}$ |
| $M = +1$ | $-\dfrac{4\zeta\tan\theta}{\beta\tilde{E}_0}$ | $-\dfrac{4\delta k\,\mathcal{M}(\tilde{e}_y - \tilde{e}_z\tan\theta)}{\beta\tilde{E}_0^2}$ | $-\dfrac{4e_z\phi\tan\theta}{\tilde{E}_0}$ |

and ellipticity terms have opposite signs for $M = \pm 1$, their contributions to $\mathcal{K}$ cancel, while the contributions from $r_M^{(APV)}$ add.

The Stark contribution, $r_M^{(Stark)}$, has several terms that are produced due to different imperfections, and it impacts all three Zeeman components, $M = 0, \pm 1$. To determine which terms could potentially mimic the PV asymmetry in $\mathcal{K}$, we discriminate the PV contribution to $\mathcal{K}$ with respect to the $B$-field reversal and flip of the polarization angle $\theta$. Switching to a different Zeeman component of the transition is also a reversal, which is incorporated in the expression for the asymmetry, $\mathcal{K}$. Analysis of the noise affecting the accuracy of PV-asymmetry measurements demonstrate that the highest signal-to-noise ratio is achieved when $\theta = \pm\pi/4$, and therefore, the polarization flip is a change of the polarization angle by $\pi/2$. Thus, the normalized-amplitude combination (14) must be determined for four different combinations of the $B$-field directions and light-polarization angles: $\mathcal{K}(+B, +\pi/4)$, $\mathcal{K}(-B, +\pi/4)$, $\mathcal{K}(+B, -\pi/4)$, and $\mathcal{K}(-B, -\pi/4)$, so that terms having different symmetries with respect to the reversals can be isolated:

$$\begin{bmatrix} \mathcal{K}_1 \\ \mathcal{K}_2 \\ \mathcal{K}_3 \\ \mathcal{K}_4 \end{bmatrix} = \frac{1}{4} \begin{bmatrix} -1 & -1 & +1 & +1 \\ -1 & +1 & +1 & -1 \\ +1 & -1 & +1 & -1 \\ +1 & +1 & +1 & +1 \end{bmatrix} \cdot \begin{bmatrix} \mathcal{K}(+B, +\theta) \\ \mathcal{K}(-B, +\theta) \\ \mathcal{K}(+B, -\theta) \\ \mathcal{K}(-B, -\theta) \end{bmatrix}. \quad (20)$$

The result of this procedure is summarized in Table II.

The PV asymmetry contributing to $\mathcal{K}_1$ is $B$-field even, $\theta$-flip odd. It competes with the second-order terms that are a combination of the $E$-field and $B$-field alignment imperfections and stray fields. Using the theoretical value of $\zeta \simeq 10^{-9}e\,a_0$ [14,15] combined with the measured $|\beta| = 2.24^{+0.07}_{-0.12} \times 10^{-8}e\,a_0/(V/cm)$ [4,7], the expected PV asymmetry, $16\zeta/\beta\tilde{E}$, is $\sim 4 \times 10^{-4}$, for $\theta = \pi/4$ and $\tilde{E}_0 = 2$ kV/cm. For a typical value of misalignments and "parasitic" fields,

TABLE II. Lowest-order terms contributing to the asymmetry $\mathcal{K}$ for $|\theta| = \pi/4$ sorted with respect to their response to the reversals. $\mathcal{K}_4$ corresponding to a rather long list of terms that are invariant with respect to all reversals is not shown.

| $\mathcal{K}_1$ | $\mathcal{K}_2$ | $\mathcal{K}_3$ |
|---|---|---|
| $\dfrac{8(\tilde{e}_y e_z + \tilde{e}_z e_y)}{\tilde{E}_0^2} + \dfrac{16\tilde{b}_x e_y}{B\tilde{E}_0} + \dfrac{16\zeta}{\beta\tilde{E}_0}$ | $\dfrac{16b'_x e_y}{B\tilde{E}_0}$ | $\dfrac{16b'_x e_z}{B\tilde{E}_0}$ |

$e_{y,z}/\tilde{E}_0$ and $\tilde{b}_x/B$ (on the order of $10^{-3}$ in the present apparatus), the contribution of the "parasitic" terms may be up to a few percent of the total value of $\mathcal{K}_1$. Ways of measuring the contribution of these imperfections are discussed in the following sections.

## V. EXPERIMENTAL APPARATUS

The forbidden 408-nm transition is excited by resonant laser light coupled into the power-buildup cavity in the presence of the magnetic and electric fields. The transition rates are detected by measuring the population of the $^3P_0$ state, where 65% of the atoms excited to the $^3D_1$ state decay spontaneously (Fig. 1). This is done by resonantly exciting the atoms with 649-nm light to the $6s7s\,^3S_1$ state downstream from the main interaction region, and by collecting the fluorescence resulting from the decay of this state to the $^3P_1$ and $^3P_2$ states and subsequently, from the decay of the $^3P_1$ state to the ground state $^1S_0$ (556-nm transition). As long as the 408-nm transition is not saturated, the fluorescence intensity measured in the probe region is proportional to the rate of that transition.

A schematic of the Yb-APV apparatus is shown in Fig. 2. A beam of Yb atoms is produced (inside of a vacuum chamber with a residual pressure of $\approx 3 \times 10^{-6}$ Torr) with an effusive source: a stainless-steel oven loaded with Yb metal, operating at 500°–600°C. The oven is outfitted with a multislit nozzle, and an external vane collimator reduces the spread of the atomic beam in the horizontal direction. The resulting Doppler width of the 408-nm transition is $\approx 12$ MHz [7].

Downstream from the collimator, the atoms enter the main interaction region where the Stark- and PV-induced transitions take place. Up to 80 mW of light at the transition wavelength of 408.345 nm in vacuum is produced by frequency doubling the output of a Ti:sapphire laser (Coherent 899) using the WaveTrain cw ring-resonator doubler. After shaping and linearly polarizing the laser beam, $\approx 10$ mW of the 408-nm radiation is coupled into a power buildup cavity (PBC) inside the vacuum chamber.

The cavity was designed to operate as an asymmetric cavity with a flat input mirror and a curved back mirror with a 25-cm radius of curvature and 22-cm separation between the mirrors. The atomic beam intersects the cavity mode in the middle of the cavity, where the $1/e^2$ radius of the mode in intensity is 172 $\mu$m. The asymmetric configuration has the advantage of a larger mode radius at the interaction position compared to a symmetric cavity. A larger mode allows us to reduce the ac Stark shifts, consequently reducing the width of the 408-nm transition. Alternatively, the cavity can be modified to operate in the symmetric confocal condition, where multiple transverse modes can be excited, thereby increasing the effective "mode" size. However, we were unable to obtain high power and stable lock for the confocal configuration.

The cavity mirrors were purchased from Research Electro Optics, Inc. For the flat input mirror, the transmission is 350 ppm with the absorption and scattering losses of 150 ppm total at 408 nm. The curved back mirror is designed to have a lower transmission of 50 ppm in order to additionally suppress the net light wave vector and, therefore, the $M1$ transition amplitude. The absorption and scattering losses in the curved mirror are 120 ppm. The finesse and the
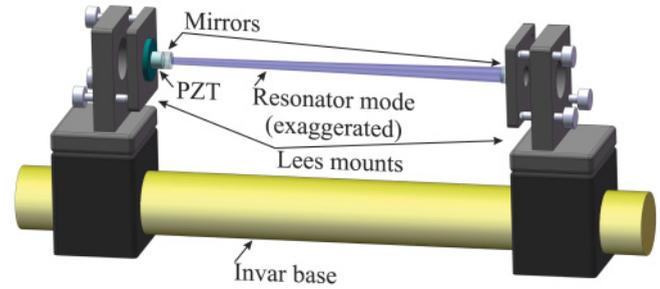


FIG. 4. (Color online) Schematic of the power buildup cavity.

circulating power of the PBC are up to $\mathcal{F} = 9000$ and $P = 8$ W. These parameters were routinely monitored during the PV measurements. Details of the characterization of the PBC are addressed in Appendix B.

We found that the use of the 408-nm PBC in vacuum is accompanied by substantial degradation of the mirrors. Typically after 6 h of operation, the finesse drops by a factor of 2. This is a limiting factor for the duration of the measurement run. The degradation of the finesse is due to the increased absorption and scattering losses. This effect is reversible: the mirror parameters can be restored by operating the PBC for several minutes in air, which makes performing a number of runs possible without replacing the mirrors. However, it takes several hours with the present apparatus to reach the desired vacuum after exposing the PBC to air. Presently, this effect is under investigation, aiming for longer duration experiments and shorter breaks in between.

A schematic of the PBC setup is presented in Fig. 4. The mirrors are mounted on precision optical mounts (Lees mounts) with micrometer adjustments for the horizontal and vertical angles and the pivot point of the mirror face. The mirror mounts are attached to an Invar rod supported by an adjustable table resting on lead blocks. The input mirror is mounted on a piezo-ceramic transducer allowing cavity scanning.

The laser is locked to the PBC using the FM-sideband technique [16]. To remove frequency excursions of the PBC in the acoustic frequency range, the cavity is locked to a more stable confocal Fabry-Pérot étalon, once again using the FM-sideband technique. This stable scannable cavity provides the master frequency, with the power buildup cavity serving as the secondary master for the laser. A schematic of the optical system is presented in Fig. 5.

The magnetic field is generated by a pair of rectangular coils designed to produce a magnetic field up to 100 G with a 1% nonuniformity over the volume with the dimensions of $1 \times 1 \times 1$ cm$^3$ in the interaction region. Additional coils placed outside of the vacuum chamber compensate for the external magnetic fields down to 10 mG at the interaction region. The residual $B$ field of this magnitude does not have an impact on the PV measurements, since its contribution is discriminated using the field reversals.

The electric field is generated with two wire-frame electrodes separated by 2.1 cm (see Fig. 6). The copper electrode frames support arrays of 0.2-mm-diameter gold-plated wires. This design allows us to reduce the stray charges accumulated on the electrodes by minimizing the surface area facing the atomic beam, thereby minimizing stray electric fields. An
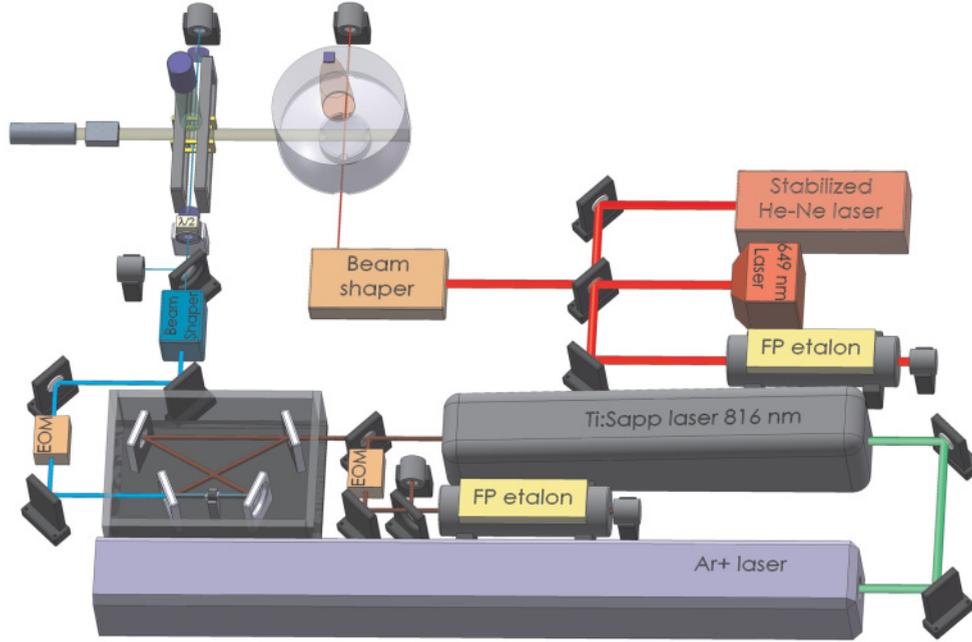
FIG. 5. (Color online) Schematic of the optical setup. Light at 408 nm is produced by frequency doubling the output of a Ti:sapphire laser (Coherent 899) using the WaveTrain cw ring-resonator doubler. The laser is locked to the PBC using the FM-sideband technique. The PBC is locked to a confocal Fabry-Pérot étalon. This scannable étalon provides the master frequency. The 649-nm excitation light is derived from a single-frequency diode laser (New Focus Vortex). The diode laser is locked to a frequency-stabilized He-Ne laser using another scanning Fabry-Pérot étalon.

ac voltage of up to 10 kV at a frequency of 76.2 Hz is supplied to the electrodes via a high-voltage amplifier. An additional dc-bias voltage of up to 100 V can be added.

The result of the electric field nonuniformity calculations is shown in Fig. 6. These calculations demonstrate that errors in the centering of the light beam with respect to the $E$-field plates may induce substantial parasitic components as large as, for example, $|e_z| \sim 5 \times 10^{-3} \tilde{E}_0$, producing parasitic effects comparable to the PV asymmetry. To measure and/or compensate for the impact of the parasitic fields, additional electrodes designed to simulate stray $E$-field components were added to the interaction region. By applying high voltage to these electrodes ("correction electrodes" in Fig. 6), the parasitic-field components may be exaggerated and accurately measured as described in the following sections.

Light at 556 nm emitted from the interaction region is collected with a light guide and detected with a photomultiplier tube. This signal is used for initial selection of the atomic resonance and for monitoring purposes. Fluorescent light from the probe region is collected onto a light guide using two optically polished curved aluminum reflectors and registered with a cooled photodetector (PD). The PD consists of a large-area ($1 \times 1$ cm$^2$) Hamamatsu photodiode connected to a 1-G$\Omega$ transimpedance preamplifier, both contained in a cooled housing (temperatures down to $-15$°C). The preamplifier's bandwidth is 1 kHz and the output noise is $\sim 1$ mV (rms). The 649-nm excitation light is derived from a single-frequency diode laser (New Focus Vortex) producing $\approx 1.2$ mW of cw output, high enough to saturate the $6s6p\,^3P_0 \rightarrow 6s7s\,^3S_1$ transition. Due to the saturation of this transition, $\sim 3$ fluorescence photons per atom exited to the $^3P_0$ state are emitted at

the probe region. The natural width of the 649-nm transition is 70 MHz, thus, its profile covers all transverse velocity groups ($v_x$) in the atomic beam ($\approx 8$ MHz Doppler width at 649 nm). A drift of the laser frequency ($\sim 100$ MHz min$^{-1}$) is eliminated by locking the diode laser to a frequency-stabilized He-Ne laser using a scanning Fabry-Pérot étalon with the scanning rate of 25 Hz. The spectral distance between the étalon transmission peaks from the two lasers is measured during each scan and maintained constant within an accuracy of $\pm 3$ MHz, good enough to eliminate any degradation of the probe-region signal.

The signals from the PMT and PD are fed into lock-in amplifiers for frequency discrimination and averaging. A typical time of a single spectral-profile acquisition is 20 s. The signals at the first and second harmonic of the electric-field modulation frequency are registered simultaneously, which reduces the influence of slow drifts, such as instabilities of the atomic-beam flux. The modulation frequency is limited by several factors. Thermal distribution of atomic velocities in the beam causes a spread (of $\approx 2$ ms) in the time of flight between the interaction region and the probe region. This, along with the finite bandwidth of the PD, leads to a reduction of the signal-modulation contrast (see below). The choice of the modulation frequency of 76.2 Hz is a tradeoff between this contrast degradation and the frequent $E$-field reversal.

## VI. RESULTS AND ANALYSIS

In Fig. 7 a profile of the $B$-field-split 408-nm spectral line of the $^{174}$Yb is shown. The 649-nm-light-induced fluorescence was recorded during a single profile scan. Statistical error bars
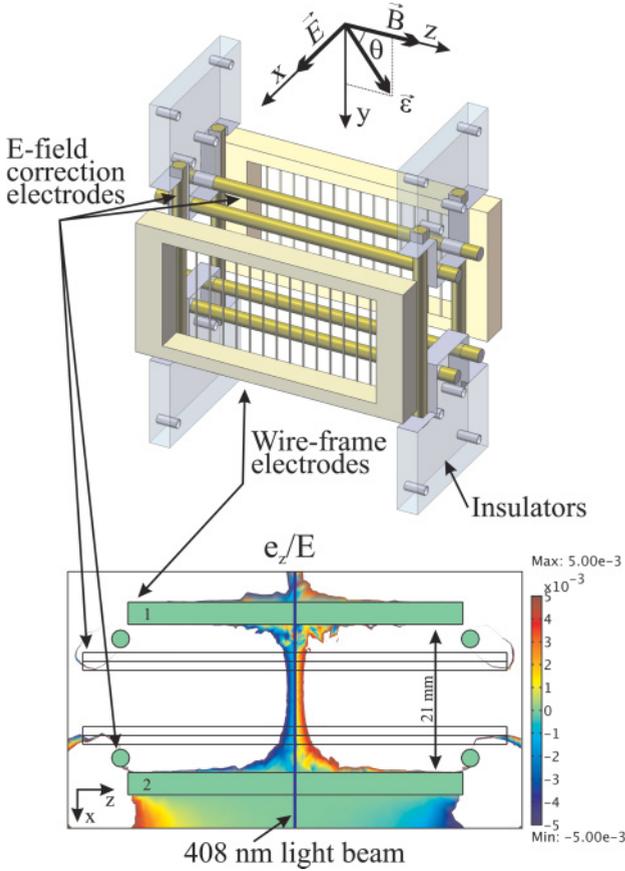
FIG. 6. (Color online) Schematic of the $E$-field electrodes assembly, and a result of the $E$-field modeling showing an $X$-$Z$ slice of the amplitude of the $E$-field $z$ component $e_z$ in a midplane ($Y = 0$) of the assembly normalized by the total $E$-field amplitude $E$. The voltage is applied to electrode 1, and electrode 2 and the correction electrodes are grounded.

determined directly from the spread of data are smaller than the points in the figure. The peculiar asymmetric line shape of the Zeeman components is a result of the dynamic Stark effect [7]. During a typical experimental run, 100 profiles are recorded for each combination of the magnetic field and the
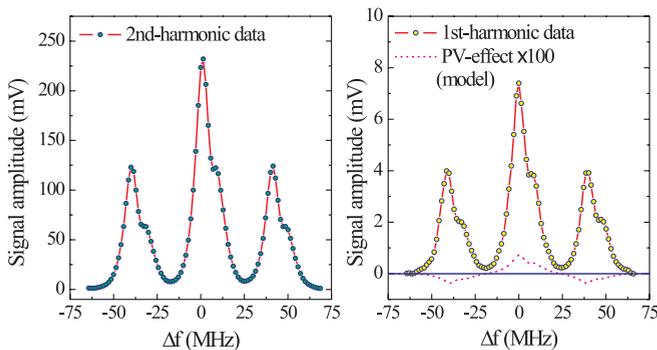


FIG. 7. (Color online) Profile of the $B$-field-split 408-nm spectral line of $^{174}$Yb recorded at first and second harmonic of the modulation. Also shown is a simulated PV contribution in the first-harmonic signal. $\tilde{E} = 5$ kV/cm; dc offset = 40 V/cm; $\theta = \pi/4$; the effective integration time is 200 ms per point.

TABLE III. Results of measurements of the electric-field imperfections using artificially exaggerated ac and dc components, $\tilde{e}^{\mathrm{ex}}_{y,z}$ and $e^{\mathrm{ex}}_{y,z}$. These fields were generated by use of the correction electrodes, see Fig. 6. $\tilde{E}_0 = 2000(2)$ V/cm.

| dc set | ac set |
|---|---|
| Exaggerated imperfections (V/cm) | |
| $e^{\mathrm{ex}}_y = -140(2)$ | $\tilde{e}^{\mathrm{ex}}_y = -120(2)$ |
| $e^{\mathrm{ex}}_z = 20(2)$ | $\tilde{e}^{\mathrm{ex}}_z = 30(2)$ |
| Measurements (mV/cm) | |
| $\tilde{e}_y \dfrac{e^{\mathrm{ex}}_z}{2\tilde{E}_0} = 16(10)$ | $e_y \dfrac{\tilde{e}^{\mathrm{ex}}_z}{2\tilde{E}_0} = 4(5)$ |
| $\left(2\tilde{E}_0 \dfrac{\tilde{b}_x}{B} + \tilde{e}_z\right) \dfrac{e^{\mathrm{ex}}_y}{2\tilde{E}_0} = 442(10)$ | $e_z \dfrac{\tilde{e}^{\mathrm{ex}}_y}{2\tilde{E}_0} = 40(5)$ |
| Parasitic fields (V/cm) | |
| $\tilde{e}_y = 3.2(2)$ | $e_y = 0.5(0.6)$ |
| $\left(2\tilde{E}_0 \dfrac{\tilde{b}_x}{B} + \tilde{e}_z\right) = -12.6(0.3)$ | $e_z = -1.3(0.2)$ |

polarization angle (400 profile scans in total). To compute the normalized amplitude $r_q$ of a selected Zeeman component, the actual first-harmonic signal near the Zeeman peak is divided by the respective second-harmonic signal and then averaged over a number of the data points.[1] Then, the combination $\mathcal{K}$ of Eq. (14) is computed for each profile scan followed by averaging the result over all the scans at a given $B$-$\theta$ configuration. This procedure is repeated for all four reversals, and all $B$-$\theta$ symmetrical contributions, $\mathcal{K}_{1-4}$, are determined. In the present experiment, the values of $\mathcal{K}_{2,3,4}$ terms are found to be consistent with zero within the statistical uncertainty, which is the same as that of the PV asymmetry (see below).

As can be seen from Table II, terms in $\mathcal{K}_1$ associated with the field imperfections are of crucial importance:

$$\frac{16}{\tilde{E}_0}\left[e_y\left(\frac{\tilde{e}_z}{2\tilde{E}_0} + \frac{\tilde{b}_x}{B}\right) + e_z\frac{\tilde{e}_y}{2\tilde{E}_0}\right].$$

To measure the contribution of these terms, artificially exaggerated $E$-field imperfections both static and oscillating, $e^{\mathrm{ex}}_z$, $e^{\mathrm{ex}}_y$, $\tilde{e}^{\mathrm{ex}}_y$, and $\tilde{e}^{\mathrm{ex}}_z$, were imposed by use of the "correction electrodes" (see Fig. 6), and two sets of the experiments were performed. In the first one, a dc voltage was applied to the correction electrodes, and the measurements were done reversing $e^{\mathrm{ex}}_y$ and $e^{\mathrm{ex}}_z$. These experiments yielded values of $\tilde{e}_y$ and $\tilde{e}_z + 2\tilde{E}_0\tilde{b}_x/B$. In the second set, an ac voltage modulated synchronously with the main $E$ field was applied to the correction electrodes. To reverse the sign of the parasitic terms, a $\pi$ phase shift of $\tilde{e}^{\mathrm{ex}}_y$ and $\tilde{e}^{\mathrm{ex}}_z$ with respect to the modulation signal was employed by switching the wiring of the correction electrodes. Thus, values of the dc imperfections, $e_y$ and $e_z$, were determined. The magnitudes of the applied electric fields and their distributions were calculated using a three-dimensional numerical model of the interaction region. The results of the experiments are presented in Table III.

---

[1] In the normalized-rate calculations, only data points having intensity higher that 1/3 of the respective Zeeman peak are used to avoid excessive noise from spectral regions with low signal intensity.

The net contribution of these imperfections to $\mathcal{K}_1$ in the absence of the exaggerated fields is found to be[2]

$$e_y \left( \frac{\tilde{e}_z}{2\tilde{E}_0} + \frac{\tilde{b}_x}{B} \right) + e_z \frac{\tilde{e}_y}{2\tilde{E}_0}$$
$$= -2.6(1.6)_{\text{stat.}}(1.5)_{\text{syst.}} \text{ mV/cm}. \quad (21)$$

The systematic uncertainty comes from a sensitivity of the numerical model of the $E$ field, which is used for calculating the exaggerated fields in the interaction region, to an imperfect approximation of the electrode-system geometry. These experiments suggest that this field's imperfection cannot mimic the PV effect entirely; nevertheless, it appears to be a major source of systematic uncertainty impacting the accuracy of the PV-asymmetry measurements. The most prominent contribution is given by a combined effect of the parasitic components of the electric field and the nonzero projection of the leading magnetic field on the direction of the electric field: $e_y(\tilde{e}_z/2\tilde{E}_0 + \tilde{b}_x/B)$. The PV-asymmetry parameter, $\zeta/\beta$ is obtained from the measured value of $\mathcal{K}_1$ by compensating for the influence of these magnetic- and electric-field imperfections, Eq. (21).

There is another effect that cannot, by itself, mimic the PV asymmetry but needs to be taken into account for proper calibration. This effect is related to the $E$-field modulation implemented in the present experiment. The atoms are excited to the metastable state, $6s6p\,^3P_0$, by the light beam in the interaction region and then travel $\sim 20$ cm until they are detected downstream in the probe region. Due to the spread in the time of flight between the interaction and probe regions, the phase mixing leads to a reduction of the signal modulation contrast at the probe region, and it depends on the signal-modulation frequency. Since the signal comprises two time scales of interest, first- and second-harmonic of the $E$-field modulation, the contrast reduction is different for the two. Therefore, the ratio of the signal-modulation amplitudes $r_M$, on which we base the PV-asymmetry observation, appears altered in the probe region compared to what it would be at the interaction region. The amplitude combination $\mathcal{K}$ and, therefore, the PV parameter $\zeta/\beta$ are similarly affected. In our data analysis, a correction coefficient $C_0$ is introduced, which has been calculated theoretically as

$$\left[ \frac{\zeta}{\beta} \right]_{\text{probe reg.}} = C_0 \left[ \frac{\zeta}{\beta} \right]_{\text{real}}.$$

Under present experimental conditions, coefficient $C_0$ is found to be 1.028(3), and the measured PV parameter is corrected accordingly. Principles of its derivation are given in Appendix C.

In Fig. 8, the PV interference parameter $\zeta/\beta$ is shown as determined in 19 separate runs ($\sim 60$ h of integration in total). Its mean value is $39(4)_{\text{stat.}}(3)_{\text{syst.}}$ mV/cm, which is in agreement with the theoretical predictions [14,15]. The value of the PV parameter was extracted using the expression given in the first column of Table II, taking into account the calibration correction $C_0$. Thus, $|\zeta| = 8.7 \pm 1.4 \times 10^{-10} e\, a_0$,

---

[2]Compare with the PV-asymmetry parameter $\zeta/\beta \approx 40$ mV/cm.
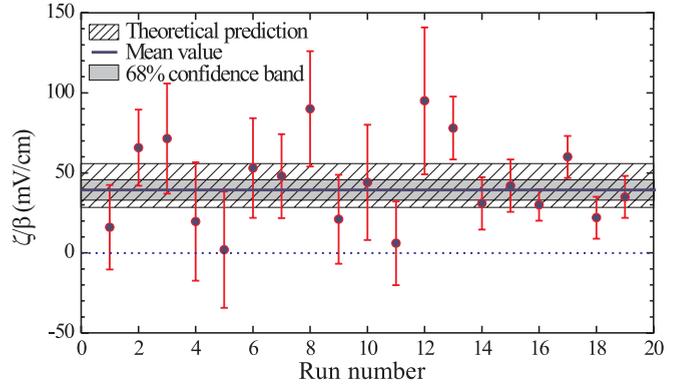


FIG. 8. (Color online) PV interference parameter $\zeta/\beta$. Mean value: $39(4)_{\text{stat.}}(3)_{\text{syst.}}$ mV/cm, $|\zeta| = 8.7 \pm 1.4 \times 10^{-10} e\, a_0$.

which is the largest APV amplitude observed so far; here we used $|\beta| = 2.24^{+0.07}_{-0.12} \times 10^{-8} e\, a_0/(\text{V/cm})$ [4,7].

The sign of the PV interference parameter $\zeta/\beta$ is found by comparing the measurements with the theoretical model of the transition rates employing the field geometry shown in Fig. 2. The direction and, thus, the signs of the electric and magnetic fields as well as the polarization angle $\theta$ were calibrated prior to the PV measurements. Special care was taken of detecting parasitic phase shifts in the lock-in amplifier. A signal from an arbitrary function direct digital synthesis (DDS) generator simulating the output of the probe region photodetector was fed into the amplifier. The signal is comprised of a sum of two sinusoidal waveforms, one frequency doubled, attenuated, and phase shifted with respect to the other. Results of the signal parameters measurement from the lock-in, such as the first-to-second harmonic amplitude ratio, relative phase shift, and its sign, are compared with those used in the DDS generator to simulate the signal. The difference in the measured and generated amplitude ratio is found to be below 0.01%, and the relative phase shift is detected within $\pm 1.5°$. No relative sign flips between the first- and second-harmonic amplitudes were detected.

## VII. ERROR BUDGET

The present measurement accuracy is not yet sufficient to observe the isotopic and hyperfine differences in the PV amplitude, which requires an accuracy better than $\approx 1\%$ for PV amplitude in a single transition [17–19]. In the present apparatus, the signal levels achieved values high enough to reach the signal-to-noise ratio (SNR) of $2/\sqrt{\tau(\text{s})}$ for the PV asymmetry if the noise were dominated by the fluorescence-photon shot noise ($\tau$ is the integration time). This is good enough to reach the sub-percent accuracy in a few hours of integration. However, a number of additional factors limit the accuracy.

One of the most important noise sources is the fluctuations of the modulating- and dc-field parameters during the experiment. The first- and the second-harmonic signals depend differently on the modulating electric-field amplitude $\tilde{E}_0$ and the dc bias; thus, a noise in the electronics controlling the fields contaminates the first-to-second harmonic ratio directly. A substantial effort was made to cope with this problem: a home-built high-voltage amplifier used in the first 13 runs
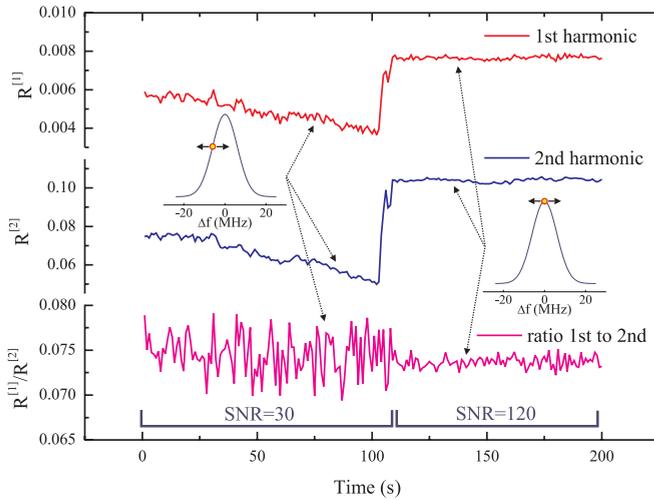
FIG. 9. (Color online) Impact of the frequency excursions of the Fabry-Pérot étalon on the noise level in the harmonics ratio. A change in the noise level when the optical system was tuned from the wing of the atomic resonance to its peak is shown. In the inserts above the excitation light spectral position is shown schematically with respect to the atomic resonance. Arrows denote the fluctuations.

was replaced by a commercial Trek 609B amplifier, and a circuit controlling the dc bias was upgraded. This allowed us to control the dc bias and $\tilde{E}_0$ with mV-scale accuracy that would make the SNR to approach the shot-noise limit if this were the only source of the noise. As seen in Fig. 8, the last six measurements exhibit higher accuracy than the rest. These are the runs after the high-voltage-system upgrade. However, the present SNR of $\approx 0.03/\sqrt{\tau(s)}$ is worse by almost two orders of magnitude than the shot-noise limit.

There are other fluctuations in the system parameters, such as light intensity fluctuations in the PBC, fluctuations of the spectral position of the PBC resonance with respect to the frequency reference, and noise in the detection system. All of them contribute to the noise in the first- and the second-harmonic signals, but we found that such noise largely canceled in the ratio $r_M$.

However, there is a noise source, which is not canceled in the ratio. The following experiments demonstrated that this noise source is related to frequency excursions of the Fabry-Pérot étalon serving as the frequency reference for the optical system. In these experiments the excitation light was frequency-tuned to a wing of the atomic resonance, and the first- and second-harmonic signals were recorded without scanning over the resonance. Then, the same was done when the spectral position was set at the peak of the resonance, and a change of the SNR for the harmonics ratio was determined. These experiments were performed using the upgraded high-voltage system. Results of the measurements are presented in Fig. 9. For a shot-noise-limited signal, the SNR at the peak of the resonance is expected to be a factor of about $\sqrt{2}$ higher than at the wing due to the larger signal. It was found, however, that the SNR went up by a factor of 4 by tuning from the wing to the peak of the resonance. This demonstrates that the main source of noise is not photon statistics but fluctuations in the spectral reference. Indeed, the frequency excursions at the wing of the spectral line produces

TABLE IV. Factors contributing to the systematic uncertainty of the PV parameter $\zeta/\beta$.

| Factor | Uncertainty (%) |
|---|---|
| $\tilde{E}$ value: | |
|     Geometry | 5 |
|     Numerical modeling | 3 |
| $E$-field imperfections | 5 |
| Phase mixing | 0.5 |
| Other | 1 |
| **Total** (in quadrature) | 8 |

substantially more intensity noise due to a steeper spectral slope than that at the peak, where the slope is nominally zero. It must be emphasized that in the case of slow frequency excursions (compared to the $E$-field modulation period), the noise in the first- and second-harmonic channels would be canceled in the ratio. However, fast excursions can generate noise in the signal ratio.

The factors affecting the measurement accuracy mentioned above have an impact on the statistical error of the result. The present systematic errors (summarized in Table IV) has nearly the same significance as the statistical one and also comprises a number of factors.

One of the most significant factors is the uncertainty in the field-imperfection contributions, Eq. (21). This uncertainty is mostly due to statistical factors such as laser drifts, nevertheless, it provides an offset to the PV parameter. Since the measurement of this contribution is actually the same measurement as the PV effect, any improvements of the stability reduces the overall systematic uncertainty. We would like to emphasize also that Eq. (21) represents a mean value of the imperfection contribution over numerous experiments averaging over possible fluctuations of the field-imperfection contribution. These fluctuations may be partially responsible for the variance in the PV parameter and, thus, the statistical uncertainty of its value. This fact demonstrates that the elimination of the field imperfections is an essential requirement for improving the overall accuracy of the experiments.

Another significant source of the systematic uncertainty is the uncertainty in the value of the electric field in the interaction region. While the voltage applied to the $E$-field plates and the correction electrodes is controlled precisely, the actual $E$-field value used in the PV parameter determination depends on the accuracy of the numerical modeling of the electric-field distribution in the particular geometry. There are two factors in the model contributing to the uncertainty: the finite accuracy of measurements of the interaction region geometrical parameters, and the imperfect approximation of the geometry in the numerical simulation.

However, while this systematic uncertainty plays a significant role for measurements of the PV parameter of a single isotope, for the isotope ratios this uncertainty will cancel (or will be substantially reduced) if the measurements observing different isotopes are performed without changing the $E$-field geometry. The same is true for the calibration parameter $C_0$, which also cancels in the isotope ratios.

There are other, rather minor, factors contributing to the systematic uncertainty, for example, a finite accuracy of the

polarization angle flip, errors in the lock-in amplifiers, a finite dynamic range of the lock-ins, etc. The net contribution of these factors is found to be $\lesssim 1\%$.

## VIII. TOWARD MEASUREMENT OF THE ISOTOPE RATIOS

As pointed out above, a goal of future measurements of the parity-violation effects in ytterbium is to observe a difference in the PV effect between different isotopes. The net uncertainty of the PV parameter of a single isotope must be better than 1% based on the theoretical predictions. To this end, a program of the apparatus upgrades and improvements is developed. Besides general improvements of the stability of the system parameters, increase of the signal levels, suppression of the electronics noise, etc., the main focus is on elimination of the frequency excursions of the frequency reference, which is a major source of the statistical noise. Improving the statistical uncertainty will contribute to more precise measurement and control of the $E$-field-imperfection contribution to the systematic part of the uncertainty. The latter is another high-priority improvement essential for reaching the goal.

In the future apparatus, the referencing of the optical system to the Fabry-Pérot étalon will be replaced by locking the system to a femtosecond frequency comb that will be available shortly. The impact of the $E$-field imperfection is planned to be substantially suppressed by redesigning the interaction region to provide more uniform and controlled electric-field distribution. Until now, no scientific or technical obstacles have been discovered preventing us from improving the apparatus to the desired level of sensitivity.

## ACKNOWLEDGMENTS

## APPENDIX A: DERIVATION OF TRANSITION AMPLITUDES

The total Hamiltonian (before including light-atom interactions and assuming **B** is along $\hat{\mathbf{z}}$) can be written as

$$H = H_{\text{Atomic}} + H_{\text{Zeeman}} + H_{\text{Stark}} + H_{\text{APV}}, \quad \text{(A1)}$$

where $H_{\text{Atomic}}$ is the atomic Hamiltonian and $H_{\text{Zeeman}}$, $H_{\text{Stark}}$, and $H_{\text{APV}}$ represent the contributions from the static magnetic field **B**, the static electric field **E**, and the parity nonconserving weak interaction, respectively. Here

$$H_{\text{Zeeman}} = -\boldsymbol{\mu} \cdot \mathbf{B} = g\mu_B \mathbf{J} \cdot \mathbf{B} = g\mu_B J_z B, \quad \text{(A2)}$$

where $\boldsymbol{\mu} = -g\mu_B \mathbf{J}$ is the magnetic dipole moment of the atom, $g$ is the Landé factor, $\mu_B$ is the Bohr magneton, and **J** is the angular-momentum operator. Similarly,

$$H_{\text{Stark}} = -\mathbf{d} \cdot \mathbf{E} = -d_i E_i, \quad \text{(A3)}$$

where **d** is the atomic electric dipole operator. Finally,

$$H_{\text{APV}} = i H_0^0, \quad \text{(A4)}$$

where $H_0^0$ is a scalar operator. Summation over repeated indices is assumed.

In the presence of a strong magnetic field, that is, when Zeeman splitting dominates Stark shifts, it is useful to think of $H_1 \equiv H_{\text{Stark}} + H_{\text{APV}}$ as a perturbation to $H_0 \equiv H_{\text{Atomic}} + H_{\text{Zeeman}}$. In this case, the $LS$-coupled states $|^{2S+1}L_J; M\rangle$, such as $|^3D_1; M\rangle$ and $|^1S_0; 0\rangle$, are eigenstates of the unperturbed Hamiltonian $H_0$. Then the first-order perturbation theory can be used to determine the eigenstates of the total Hamiltonian:

$$|\overline{a}\rangle = |a\rangle + \sum_{a'} \frac{|a'\rangle\langle a'|H_1|a\rangle}{\omega(a) - \omega(a')}, \quad \text{(A5)}$$

where $\omega(a)$ is the energy of state $|a\rangle$. (Perturbed eigenstates are denoted using an overbar.)

The electric dipole amplitude for the optical transition of interest is

$$A_M^{(E1)} = \langle^3D_1; M|(-\mathbf{d} \cdot \boldsymbol{\mathcal{E}})|^1S_0\rangle \equiv A_M^{(\text{Stark})} + A_M^{(\text{APV})}, \quad \text{(A6)}$$

where

$$A_M^{(\text{Stark})} = \sum_{a'} \frac{\langle^3D_1; M|\mathbf{d} \cdot \mathbf{E}|a'\rangle\langle a'|\mathbf{d} \cdot \boldsymbol{\mathcal{E}}|^1S_0\rangle}{\omega(^3D_1) - \omega(a')}$$
$$+ \sum_{a'} \frac{\langle^3D_1; M|\mathbf{d} \cdot \boldsymbol{\mathcal{E}}|a'\rangle\langle a'|\mathbf{d} \cdot \mathbf{E}|^1S_0\rangle}{\omega(^1S_0) - \omega(a')}, \quad \text{(A7)}$$

and

$$A_M^{(\text{APV})} = \sum_{a'} \frac{\langle^3D_1; M|i H_0^0|a'\rangle\langle a'|\mathbf{d} \cdot \boldsymbol{\mathcal{E}}|^1S_0\rangle}{\omega(^3D_1) - \omega(a')}$$
$$- \sum_{a'} \frac{\langle^3D_1; M|\mathbf{d} \cdot \boldsymbol{\mathcal{E}}|a'\rangle\langle a'|i H_0^0|^1S_0\rangle}{\omega(^1S_0) - \omega(a')}. \quad \text{(A8)}$$

The Stark amplitude can be written as

$$A_M^{(\text{Stark})} = T_{ij}\langle^3D_1; M|U_{ij}|^1S_0\rangle, \quad \text{(A9)}$$

where $T_{ij} = E_i \mathcal{E}_j$ and

$$U_{ij} = \sum_{a'} \frac{d_i|a'\rangle\langle a'|d_j}{\omega(^3D_1) - \omega(a')} + \frac{d_j|a'\rangle\langle a'|d_i}{\omega(^1S_0) - \omega(a')}. \quad \text{(A10)}$$

Let $T_q^k$ and $U_q^k$ represent the irreducible spherical components of the tensors $T_{ij}$ and $U_{ij}$. Then $T_{ij}U_{ij} = (-1)^q T_{-q}^k U_q^k$ and Eq. (A7) becomes

$$A_M^{(\text{Stark})} = (-1)^q T_{-q}^k \langle^3D_1; M|U_q^k|^1S_0\rangle$$
$$= (-1)^q T_{-q}^k \frac{(^3D_1||U^k||^1S_0)}{\sqrt{3}}\langle 0, 0; k, q|1, M\rangle$$
$$= i\beta(-1)^q(\mathbf{E} \times \boldsymbol{\mathcal{E}})_{-q}\langle 0, 0; 1, q|1, M\rangle. \quad \text{(A11)}$$

Here $\beta$ is the vector Stark transition polarizability and defined by

$$\beta \equiv \frac{1}{\sqrt{6}}(^1S_0||U^1||^3D_1). \quad \text{(A12)}$$

To derive Eq. (A11), we used $\langle 0, 0; k, q|1, M\rangle = \delta_{k1}\delta_{qM}$ and $T_{-q}^1 = \sum_{q_1,q_2}\langle 1, q_1; 1, q_2|1, -q\rangle E_{q_1}\mathcal{E}_{q_2} = (i/\sqrt{2})(\mathbf{E} \times \boldsymbol{\mathcal{E}})_{-q}$.

For the parity-violating contribution to the $E1$ transition amplitude, we can likewise write

$$A_M^{(\text{APV})} = i\mathcal{E}_i \langle {}^3D_1; M | W_i | {}^1S_0 \rangle, \tag{A13}$$

where

$$W_i = \sum_{a'} \frac{H_0^0 |a'\rangle\langle a'|d_i}{\omega({}^3D_1) - \omega(a')} - \sum_{a'} \frac{d_i|a'\rangle\langle a'|H_0^0}{\omega({}^1S_0) - \omega(a')}. \tag{A14}$$

Let $\mathcal{E}_q^1$ and $W_q^1$ represent the spherical components of the vectors $\mathcal{E}_i$ and $W_i$, respectively. Then $\mathcal{E}_i W_i = (-1)^q \mathcal{E}_{-q}^1 W_q^1$ and we have

$$
\begin{aligned}
A_M^{(\text{APV})} &= i(-1)^q \mathcal{E}_{-q}^1 \langle {}^3D_1; M | W_q^1 | {}^1S_0 \rangle \\
&= i(-1)^q \mathcal{E}_{-q}^1 \frac{\left({}^3D_1||W^1||{}^1S_0\right)}{\sqrt{3}} \langle 0,0; 1,q|1,M\rangle \\
&= i\zeta(-1)^q \mathcal{E}_{-q}^1 \langle 0,0; 1,q|1,M\rangle. \tag{A15}
\end{aligned}
$$

Here $\zeta$ is given by

$$\zeta \equiv \frac{1}{\sqrt{3}} \left( {}^3D_1 || W^1 || {}^1S_0 \right). \tag{A16}$$

## APPENDIX B: CHARACTERIZATION OF THE PBC MIRRORS

The finesse of the cavity is measured using the cavity-ring-down method [20]. The laser beam is sent through a Pockels cell (Cleveland Crystals Inc. QX 1020 Q-Switch) and a polarizer before entering the cavity. The polarizer is aligned with the laser polarization so that the light is transmitted when there is no voltage applied to the Pockels cell. A high-voltage pulse generator is used to send a fast step signal (30-ns wavefront) to the Pockels cell which rotates the polarization of the light so that it is not transmitted through the polarizer. The laser frequency is locked to the resonance frequency of the cavity, and then the Pockels cell is switched into the nontransmitting state, causing a fast interruption of the laser power. The subsequent decay of the light inside the cavity is monitored with a fast photodiode (50-MHz bandwidth) measuring the power transmitted through the back mirror of the cavity. The signal is fit to an exponential decay. The decay time is related to the finesse of the cavity $\mathcal{F}$ by

$$\mathcal{F} = \frac{\pi c}{L}\tau,$$

where $c$ is the speed of light, $L$ is the cavity length, and $\tau$ is the intensity decay time. An example of the PBC transmission signal and its fit are shown in Fig. 10.

Following the analysis discussed in [21], if we denote the transmission of mirrors 1 and 2 by $T_1$ and $T_2$, respectively, and the absorption+scatter loss per mirror as $l_{1,2} = (A+S)_{1,2}$, then the total cavity losses $\mathcal{L} = T_1 + T_2 + l_1 + l_2$ determine the finesse $\mathcal{F}$:

$$\mathcal{F} = \frac{2\pi}{T_1 + T_2 + l_1 + l_2}. \tag{B1}$$

Information on the transmission of the mirrors discriminated from the $A+S$ losses can be obtained using the measured
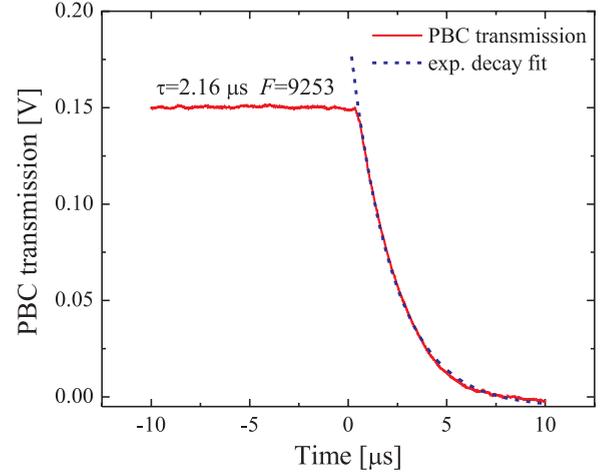


FIG. 10. (Color online) Application of the cavity-ring-down method for the determination of the finesse of PBC.

value of the finesse and the power transmitted trough PBC, $P_{\text{tr}}$:

$$\frac{P_{\text{tr}}}{\epsilon P_{\text{in}}} = 4T_1 T_2 \left( \frac{\mathcal{F}}{2\pi} \right)^2, \tag{B2}$$

where $P_{\text{in}}$ is the input power, and $\epsilon$ is a mode-matching factor. For two arbitrary mirrors, for which neither $T_{1,2}$ nor $l_{1,2}$ are known, Eqs. (B1) and (B2) do not provide a solution, since a number of variables exceeds the number of equations. Nevertheless, for two mirrors from the same coating run when one can assume that $T_1 = T_2 = T$ and $l_1 = l_2 = l$, Eqs. (B1) and (B2) become

$$
\mathcal{F} = \frac{\pi}{T+l},
$$
$$
\frac{P_{\text{tr}}}{\epsilon P_{\text{in}}} = 4T^2 \left( \frac{\mathcal{F}}{2\pi} \right)^2,
$$

and for known mode-matching factor $\epsilon$, the parameters of the mirrors ($T$ and $l$) can be determined. The factor $\epsilon$ depends on the geometry of the cavity and is assumed to stay constant upon replacement of the mirrors if the geometry of the input laser beam and the configuration of the PBC are unchanged. This gives the possibility of calibrating this factor by using a mirror set for which the transmission is known. We used for this purpose a mirror set purchased from Advanced Thin Films, Inc., for which reliable data on the transmission of the mirrors is provided by the supplier. By measuring the finesse of the PBC comprised of these mirrors and the ratio of the transmitted-to-input power, the mode-matching factor and the $A + S$ mirror losses $l$ are found. This set is not an actual mirror set that was used in the PV experiment; nevertheless, the parameters of other mirrors were determined by replacing one mirror in the "reference" set by the "test" mirror, parameters of which are sought. The geometry of the cavity was unchanged during the replacement.

## APPENDIX C: IMPACT OF THE PHASE MIXING EFFECT ON THE HARMONICS RATIO

Atoms undergo the $6s^2\,{}^1S_0 \to 5d6s\,{}^3D_1$ transition in the interaction region where they are illuminated by 408-nm light and are exposed to the static magnetic field and the oscillating

electric field $E(t)$. Excited atoms then spontaneously decay from the $5d6s\ ^3D_1$ state to the metastable $6s6p\ ^3P_0$ state. The population of $6s6p\ ^3P_0$ is proportional to the transition rate $R_M$ for $M = 0, \pm1$.

The probe region where the $6s6p\ ^3P_0$ population was measured, is located a distance $d \approx 20$ cm away from the interaction region. Therefore, an atom that arrives at the detection region at a time $t$ has experienced an electric field with magnitude $E(t - d/v_z)$ in the interaction region, where $v_z$ is the atom's speed.

Because the beam is not monokinetic, the detection region contains atoms that have experienced different electric fields while in the interaction region. Each atom contributes to the total rate, and hence the observed rate $\overline{R}_M$ is the thermal average of every contribution:

$$\overline{R}_M(t; \omega, d, v_0) = \int_0^\infty R_M(t - d/v_z) f(v_z; v_0)\, dv_z, \quad \text{(C1)}$$

where

$$f(v_z; v_0)\, dv_z = 2(v_z/v_0)^3 e^{-(v_z/v_0)^2}\, dv_z/v_0 \quad \text{(C2)}$$

is the probability for an atom to have speed between $v_z$ and $v_z + dv_z$. Here $v_0 = \sqrt{2k_B T/m} = 2.9 \times 10^4$ cm/s is the thermal speed, $T \approx 873$ K is the oven temperature, and $m \approx 161 \text{GeV}/c^2$ is the atomic mass of Yb.

It is convenient to introduce the dimensionless variables $x = v_z/v_0$ and $\tau = \omega t$, and the dimensionless parameter $\alpha = \omega d/v_0$. Then the average rate $\overline{R}_M(t; \omega, d, v_0) \to \overline{R}_M(\tau; \alpha)$ depends only on the dimensionless quantities $\alpha$ and $\tau$, and Eq. (C1) becomes

$$\overline{R}_M(\tau; \alpha) = \mathcal{R}_M^{[0]} + \mathcal{R}_M^{[1]} |I(\alpha)| \cos\{\tau + \text{Arg}[I(\alpha)]\}$$
$$+ \mathcal{R}_M^{[2]} |I(2\alpha)| \cos\{2\tau + \text{Arg}[I(2\alpha)]\}, \quad \text{(C3)}$$

with

$$I(\alpha) \equiv \int_0^\infty e^{-i\alpha/x} f(x; 1)\, dx. \quad \text{(C4)}$$

Note that $|I(\alpha)| \to 0$ as $\alpha \to \infty$, whereas $|I(\alpha)| \approx 1$ when $\alpha < 1$. This places a limit on the modulation frequency: We require that $\omega < v_0/d = 2\pi \times 230$ Hz in order to avoid a significant decrease in signal.

The lock-in amplifier receives an input signal proportional to $\overline{R}_M$ and returns two output signals $S_M^{[1]}$ and $S_M^{[2]}$ corresponding to the first- and second-harmonic components, respectively. This can be modeled as

$$S_M^{[n]}(\phi_n; \alpha) = \frac{1}{\pi} \int_0^{2\pi} \overline{R}_M(\tau; \alpha) \cos(n\tau + \phi_n)\, d\tau$$
$$= \mathcal{R}_M^{[n]} |I(n\alpha)| \cos\{\text{Arg}[I(n\alpha)] + \phi_n\}, \quad \text{(C5)}$$

where the phases $\phi_{1,2}$ of the lock-in amplifier are chosen to maximize the signals $S_M^{[1,2]}$. That is,

$$\phi_n = \phi_n(\alpha) \equiv -\text{Arg}[I(n\alpha)]. \quad \text{(C6)}$$

Our measurement $s_M$ is the ratio of the first- and second-harmonic signals:

$$s_M = \frac{S_M^{[1]}(\phi_1; \alpha)}{S_M^{[2]}(\phi_2; \alpha)} = \frac{\mathcal{R}_M^{[1]} |I(\alpha)|}{\mathcal{R}_M^{[2]} |I(2\alpha)|} = r_M \times C(\alpha), \quad \text{(C7)}$$

where $C(\alpha) \equiv |I(\alpha)|/|I(2\alpha)|$ is the *correction factor*. Therefore, we must further divide the ratio $s_M$ of observed output signals by $C(\alpha)$ to measure the ratio $r_M$.

The correction factor $C(\alpha)$ and the optimal lock-in phases $\phi_{1,2}(\alpha)$ inherit dependence on the modulation frequency ($\omega = 2\pi \times 76.2$ Hz), the distance between interaction and detection regions ($d \approx 20$ cm), and the oven temperature ($T \approx 873$ K) through the parameter $\alpha$:

$$\alpha = \frac{\omega d}{\sqrt{2k_B T/m}} = 0.33(2), \quad \text{(C8)}$$

where the uncertainty in $\alpha$ is dominated by

$$\delta\alpha = \alpha\sqrt{(\delta T/2T)^2 + (\delta d/d)^2}, \quad \text{(C9)}$$

for $\delta T \approx 50$ K and $\delta d \approx 1$ cm. The correction factor can be computed numerically and has a value

$$C_0 = C(\alpha) = 1.028(3), \quad \text{(C10)}$$

with uncertainty given by $\delta C_0 = |C'(\alpha)|\, \delta\alpha$. Likewise, the lock-in phases have the following values

$$\phi_{10} = \phi_1(\alpha) = 16(1)^\circ, \quad \phi_{20} = \phi_2(\alpha) = 33(2)^\circ, \quad \text{(C11)}$$

where $\delta\phi_{n0} = |\phi_n'(\alpha)|\, \delta\alpha$.

To understand the impact of imperfect phase selections, we include the effects of slight deviations from the optimal phase $\phi_n(\alpha)$ by taking

$$\phi_n \to \phi_n(\alpha) + \varphi_n, \quad \text{(C12)}$$

where $\varphi_n$ represents a small deviation. Then the correction factor becomes

$$C(\alpha) \to \tilde{C}(\alpha, \varphi_1, \varphi_2) = C(\alpha) \frac{\cos(\varphi_1)}{\cos(\varphi_2)}, \quad \text{(C13)}$$

and hence $\tilde{C}_0 = \tilde{C}(\alpha, 0, 0) = C(\alpha) = C_0$. The uncertainty in the correction factor becomes

$$\delta C_0 \to \delta\tilde{C}_0 = \sqrt{\delta C_0^2 + \delta\varphi_1^4 + \delta\varphi_2^4}, \quad \text{(C14)}$$

where $\delta\varphi_n$ is the uncertainty in the deviation $\varphi_n$. To derive this expression, we estimated the partial uncertainty in $\tilde{C}_0$ due to $\varphi_n$ by $\partial_{\varphi_n}^2 \tilde{C}(\alpha, \varphi_1, \varphi_2)\, \delta\varphi_n^2$.

To estimate the uncertainty $\delta\varphi_n$, we assume that we are within about $1^\circ$ of the optimal phase. This choice is consistent with the magnitude of the uncertainty in the optimal phases $\phi_{10}$ and $\phi_{20}$. Therefore, we will take $\delta\varphi_n = \delta\phi_{n0}$ to be the accuracy with which we can select the lock-in phases. Then $\delta\varphi_1 = 0.02$, $\delta\varphi_2 = 0.03$, and

$$\delta\tilde{C}_0 = 0.0031 \approx 0.0029 = \delta C_0. \quad \text{(C15)}$$

Hence small deviations (on the order of $1^\circ$) have a negligible effect on the uncertainty in the correction factor.

[1] K. Tsigutkin, D. Dounas-Frazer, A. Family, J. E. Stalnaker, V. V. Yashchuk, and D. Budker, Phys. Rev. Lett. **103**, 071601 (2009).

[2] D. DeMille, Phys. Rev. Lett. **74**, 4165 (1995).

[3] C. J. Bowers, D. Budker, E. D. Commins, D. DeMille, S. J. Freedman, A. T. Nguyen, S. Q. Shang, and M. Zolotorev, Phys. Rev. A **53**, 3103 (1996).

[4] C. J. Bowers, D. Budker, S. J. Freedman, G. Gwinner, J. E. Stalnaker, and D. DeMille, Phys. Rev. A **59**, 3513 (1999).

[5] J. E. Stalnaker, D. Budker, D. P. DeMille, S. J. Freedman, and V. V. Yashchuk, Phys. Rev. A **66**, 031403(R) (2002).

[6] D. Budker and J. E. Stalnaker, Phys. Rev. Lett. **91**, 263901 (2003).

[7] J. E. Stalnaker, D. Budker, S. J. Freedman, J. S. Guzman, S. M. Rochester, and V. V. Yashchuk, Phys. Rev. A **73**, 043416 (2006).

[8] D. F. Kimball, D. Clyde, D. Budker, D. DeMille, S. J. Freedman, S. Rochester, J. E. Stalnaker, and M. Zolotorev, Phys. Rev. A **60**, 1103 (1999).

[9] B. DeBoo, D. F. Kimball, C. H. Li, and D. Budker, J. Opt. Soc. Am. B **18**, 639 (2001).

[10] D. F. Kimball, Phys. Rev. A **63**, 052113 (2001).

[11] M. A. Bouchiat and C. Bouchiat, J. Phys. I **36**, 493 (1975).

[12] R. Conti, P. Bucksbaum, S. Chu, E. D. Commins, and L. Hunter, Phys. Rev. Lett. **42**, 343 (1979).

[13] D. Budker, D. Kimball, and D. DeMille, *Atomic Physics. An Exploration Through Problems and Solutions*, 2nd ed. (Oxford University, New York, 2008).

[14] S. G. Porsev, M. G. Kozlov, and Yu. G. Rakhlina, Hyperfine Interact. **127**, 395 (2000).

[15] B. P. Das, Phys. Rev. A **56**, 1635 (1997).

[16] R. W. P. Drever, J. L. Hall, F. V. Kowalski, J. Hough, G. M. Ford, A. J. Munley, and H. Ward, Appl. Phys. B **31**, 97 (1983).

[17] B. A. Brown, A. Derevianko, and V. V. Flambaum, Phys. Rev. C **79**, 035501 (2009).

[18] S. Porsev, M. Kozlov, and Y. Rakhlina, Hyperfine Interact. **127**, 395 (2000).

[19] A. D. Singh and B. P. Das, J. Phys. B **32**, 4905 (1999).

[20] D. Z. Anderson, J. Frisch, and C. S. Masser, Appl. Opt. **23**, 1238 (1984).

[21] C. J. Hood, H. J. Kimble, and J. Ye, Phys. Rev. A **64**, 033804 (2001).